PAPER

Check for updates

3D printed bioceramic scaffolds with fully interconnected channel networks for enhanced vascularized bone regeneration†

Tao Zhang,‡[a,b] Lifei Huang,‡[c] Xiaonan Zhang,[c] Jiali Guo,[c] Yunming Shen[a,b] and Yongxiang Luo [ID] *[c]

Bioceramics have emerged as some of the most widely utilized and promising biomaterials for bone repair. The structural morphology of bioceramic scaffolds plays a critical role in determining their overall performance. Strategic morphological design and optimization have been demonstrated to substantially augment therapeutic outcomes. Herein, in this study, we present a strategy for fabricating β-tricalcium phosphate (β-TCP) bioceramic scaffolds featuring a dual-pore architecture comprising fully interconnected hollow channel networks and open macropores, achieved through extrusion-based 3D printing coupled with surface crosslinking. The manufacturing process enables simultaneous structural optimization and bioactive ion incorporation (*e.g.*, Cu^{2+}, Sr^{2+}) during surface crosslinking. Comparative *in vitro* and *in vivo* evaluations revealed that the interconnected channel system significantly enhanced mass transport efficiency and cellular infiltration, leading to superior bone tissue ingrowth and vascularization compared to both non-channeled scaffolds and those with non-interconnected channels fabricated by coaxial 3D printing. This work establishes the following advances: integration of macropores with fully interconnected channel networks in bioceramic scaffolds using extrusion-based additive manufacturing, and demonstration of enhanced vascularized osteogenesis through optimized structural design. The findings provide insights into the rational design of advanced bioceramic scaffolds for functional bone regeneration.

1. Introduction

Scaffold-based bone tissue engineering is still one of the most promising strategies to repair bone defects,[1] caused by trauma, tumor resection and congenital deformities. In the process, the physical architecture and chemical composition of three dimensional (3D) porous scaffolds hold paramount significance in promoting vascularization and bone regeneration.[2,3] It is well known that the biological functions of cells and tissues are regulated by various biochemical factors. Meanwhile, in the field of tissue engineering, the physical cues exhibited by biomaterials and scaffolds occupy an important position as they significantly influence cellular

behaviors and tissue regeneration processes.[4] For instance, the surface micro/nano architectures of biomaterials could regulate cell adhesion, proliferation and differentiation.[5,6] The porosity and pore size of scaffolds have been widely demonstrated to critically influence bone regeneration.[7] Additionally, the pore architecture also serves as a crucial determinant in regulating cellular behavior, vascularization and bone tissue formation. Specifically, previous studies have highlighted the significance of hollow channels in offering vital architectural cues for tissue engineering.[8–10] For example, the hollow channels could enhance cell infiltration, delivering oxygen and nutrients to the bulk of scaffolds, and promote the integration of host tissues and the invasion of blood vessels *in vivo*.[11] Furthermore, the hollow channels also have roles in patterning cells and controlling the spatiotemporal distribution of molecules and ligands in the 3D scaffolds.[12] Therefore, scaffolds incorporating hollow channels emerge as a promising alternative strategy to tackle the challenges of sluggish vascularization and inadequate new bone tissue formation encountered in the repair of large bone defects.

Various methods have been developed to prepare hollow channeled scaffolds, such as the conventional methods using array templates.[13] However, these conventional methods often

[a]Department of Medical Equipment, Children's Hospital, Zhejiang University School of Medicine, Hangzhou, 310057, China
[b]National Clinical Research Center for Child Health, Hangzhou, 310057, China
[c]Guangdong Key Laboratory for Biomedical Measurements and Ultrasound Imaging, Department of Biomedical Engineering, Shenzhen University Medical School, Shenzhen University, Shenzhen 518055, China. E-mail: luoyongxiang@szu.edu.cn
†Electronic supplementary information (ESI) available. See DOI: https://doi.org/10.1039/d5bm00824g
‡These authors contributed equally to this work.

fall short in their ability to precisely control the morphology of the scaffold. 3D printing with the apparent merits of individual design and precise control is a powerful technique to fabricate 3D porous scaffolds for tissue engineering,[14–16] including scaffolds with designed hollow channels.[17] For instance, alginate based hydrogel scaffolds with macro pores and hollow channels were fabricated by co-axial 3D printing.[18] Moreover, hollow channeled bioceramic scaffolds have also been fabricated using this method. In our previous study, we created silicate-based bioceramic scaffolds with hollow channels using co-axial 3D printing and the hollow channels showed architectural cues for promoting new bone formation *in vivo*.[19,20] However, although co-axial 3D printing is an efficient and direct approach to prepare hollow channels in scaffolds, the created hollow channels were not interconnected. Extensive research has convincingly demonstrated the critical importance of the interconnection between macro pores within 3D scaffolds for successful bone repair.[21,22] Insufficient pore interconnection can hinder fluid diffusion and cell migration, ultimately impeding vascularization and the formation of new bone tissues within the scaffolds. Additionally, it is still a challenge to create branched tubular structures using this method. Another approach utilizing fugitive materials for creating hollow channels within scaffolds is also widely reported.[23–25] While this methodology effectively enables the creation of fully interconnected hollow channels, it falls short of concurrently achieving controlled macro pores within the scaffolds. Furthermore, its applicability appears to be limited primarily to the fabrication of hydrogel scaffolds.

Recently, we reported a novel method to fabricate hydrogel scaffolds with macro pores and fully interconnected hollow channels using 3D printing and surface crosslinking.[26,27] The fully interconnected hollow channels showed excellent performance to facilitate the formation of vessels not only in the periphery but also in the center of the hydrogel scaffolds. However, hydrogel scaffolds still face the challenge of poor mechanical properties and a lack of bioactivity for bone repair applications.[28] In addition, the swelling behavior of hydrogels adversely affects their structural stability, creating undue pressure and potential damage to the surrounding tissues, which further restricts their application in critical sized bone defect repair.[29] Bioceramics have garnered widespread adoption in bone tissue engineering, not only due to their commendable structural and mechanical stability and excellent bioactivity but also because they exhibit the ability to promote vascularization and bone healing *via* the release of vital bioactive ions like silicon, copper, strontium, and manganese.[30–32] However, fabrication of bioceramic scaffolds with precisely designed macro pores and meticulously controlled morphology such as fully interconnected hollow channels, a feature that could potentially amplify their efficacy, has yet to be fully addressed and optimized.

Herein, in this study, we successfully fabricated β-tricalcium phosphate (β-TCP) scaffolds containing both macro pores and fully interconnected hollow channel networks by 3D printing and surface crosslinking. During the cross-linking process, precisely controlled doping of select trace elements, including copper and strontium ions, was achieved within the scaffolds, thereby enhancing their overall performance. The copper/strontium ion doped β-TCP scaffolds with fully interconnected hollow channels (CSH) exhibited remarkable synergistic effects in advancing vascularized bone repair (Fig. 1). This was achieved through the controlled release of bioactive ions and the provision of optimal architectural cues, fostering a conducive environment for bone regeneration. The *in vivo* results demonstrated that the CSH scaffolds significantly promoted rapid vascularization and bone formation not only in the periphery but also in the center of the scaffolds after implantation in critical-sized skull defects in rats.

2. Experimental section

2.1 Materials

Calcium phosphate (β-TCP) was purchased from Kunshan Overseas Chinese Technology New Materials Corporation (China). Sodium alginate from brown algae and gelatin from porcine skin were purchased from Sigma-Aldrich (USA). Cupric chloride ($CuCl_2$) with 98% purity, calcium chloride ($CaCl_2$) with 96% purity, and strontium chloride ($SrCl_2$) with 98% purity were obtained from Shanghai Macklin Biochemical Co., Ltd, China.

2.2 Preparation and characterization of CSH scaffolds

Sodium alginate powder (1 g) and β-TCP powder (2 g) were mixed and ground using a mortar. Subsequently, the homogeneous mixture was dispersed in a 9 wt% gelatin solution (8 mL) and stirred to form a paste, serving as the printing ink. The bioceramic scaffolds with a pre-designed structure were fabricated using a 3D printing system (BioScaffolder 3.1 from GeSiM, Germany) at a printing speed of 5–7 mm s^{-1} and a dosing pressure of 200–250 kPa. The printing temperature was set at 60 °C. The scaffolds were then transferred to crosslinking solutions (0.1 M $CuCl_2$ and $SrCl_2$) for 5 min. Then, the ends of the scaffolds were excised and immersed in deionized water (60 °C) to remove uncrosslinked materials from the center of the printed filaments. Then, scaffolds with macro pores and fully interconnected channel networks were obtained. After drying, the scaffolds underwent sintering at 1100 °C for 180 min at a heating rate of 2 °C min^{-1} as reported previously.[33] Then, copper/strontium ion doped β-TCP scaffolds with fully interconnected hollow channels, abbreviated as CSH scaffolds, with enhanced structural stability and mechanical properties were achieved. The effects of different crosslinking solutions and crosslinking time periods (5, 10, and 15 min) on the formation of hollow channels were investigated in detail. Subsequently, the scaffolds were characterized using microscopy (TOKYO 16 3-0914, Japan), scanning electron microscopy (SEM, FEI APREO S, Thermo Scientific, the Netherlands), and X-ray diffractometry (XRD, D8 VENTURE, Bruker).

The control samples were also prepared as follows: (a) for CSS, the copper/strontium ion doped β-TCP scaffolds without
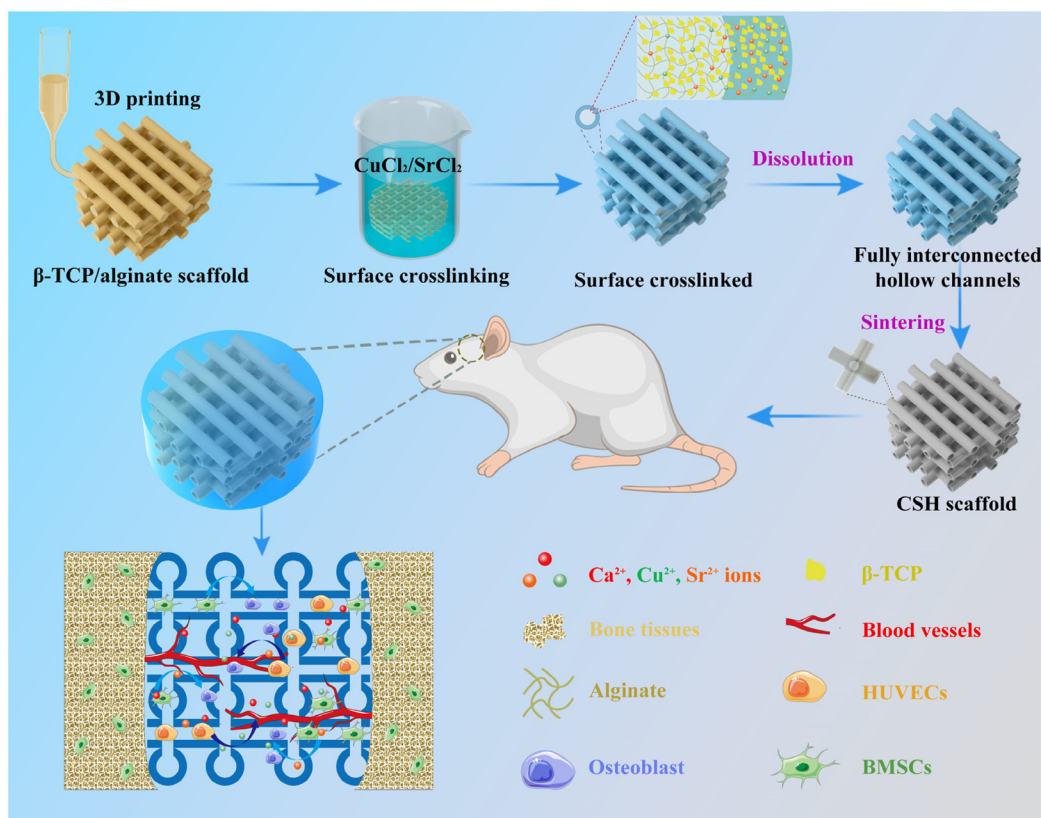
Fig. 1 The fabrication scheme involves creating a Cu/Sr-doped β-TCP scaffold with macro pores and fully interconnected hollow channel networks using 3D printing and surface crosslinking techniques. The interconnected hollow channels, in conjunction with the released bioactive ions, exhibit an enhanced ability to promote vascularization and new bone formation.

hollow channels, the scaffold was crosslinked with a 0.1 M mixture of $CuCl_2$ and $SrCl_2$. However, a crucial step was omitted—the removal of uncrosslinked materials from the core of the printed filaments; then the scaffold with solid filaments (non-hollow) was obtained. (b) For CSC, the copper/strontium ion doped β-TCP scaffold with non-interconnected hollow channels, the scaffolds were prepared by co-axial 3D printing, and then crosslinked by 0.1 M $CuCl_2$/$SrCl_2$ solution. So, a CSC scaffold with unconnected hollow channels was obtained (Table 1).

The potential cellular infiltration pathways from the open ends of channels to the central regions of CSH and CSC scaffolds were simulated using COMSOL Multiphysics software. The computational modeling process involved three main steps: (1) establishing the geometric model of the scaffold structure, (2) selecting appropriate physical fields for the simulation, and (3) systematically configuring the relevant parameters to accurately represent the cell infiltration process.

2.3 The measurement of porosity, mechanical properties and the *in vitro* degradation of the scaffolds

The porosity of the prepared scaffold was measured according to Archimedes' principle. Briefly, the scaffold was weighed in the dry state (W_1); then, the scaffold was prewetted with ethanol, and the weight of the scaffold suspended in water (W_2) was measured. The fully water-saturated scaffold (W_3) was weighed again in air. The measurements were conducted at

Table 1 The differences among CSS, CSC and CSH scaffolds

	CSH	CSC	CSS
Structure	Macro pores + fully interconnected hollow channels	Macro pores + non-interconnected hollow channels	Macro pores
Preparing methods	3D printing + surface crosslinking	Co-axial 3D printing	3D printing
Porosity	83.6 ± 3.4%	78.2 ± 2.8%	56.5 ± 3.8%
Compressive strength (MPa)	1.15 ± 0.29	1.22 ± 0.31	3.42 ± 0.25
Modulus (MPa)	36.41 ± 4.67	38.51 ± 5.83	66.72 ± 5.23

room temperature, and the porosity was calculated according to the following equation:

$$P = (W_3 - W_1)/(W_3 - W_2) \times 100\%$$

The compressive strength and modulus of the dry scaffolds ($10 \times 10 \times 5$ mm, $n = 5$) were evaluated utilizing a universal testing machine (CMT5504, MTS Systems, China), which was equipped with a 50 kN load cell, under room temperature conditions in accordance with the ISO 13314 standard. Quasi-static tests were conducted at a rate of 1 mm min^{-1}, and the tensile modulus was subsequently determined according to the slope of the strain–stress curves. To assess the *in vitro* degradation of the scaffolds, samples ($n = 5$) were immersed in Tris-hydrochloride (Tris-HCl, pH 7.4) solution and then kept in a shaker (37 °C, 150 rpm). The Tris-HCl solution was refreshed weekly. At specific time intervals (1, 3, 7, 14, 21, 28, 42, 56, and 70 days), the scaffolds were retrieved and thoroughly dried, and then their weight loss was quantified using a microbalance. Additionally, at these designated time points (1, 7, 14, 21 and 28 days), the release of bioactive ions from the scaffolds was precisely measured utilizing an Avio 200 ICP-OES system from PerkinElmer Inc., USA.

2.4 Proliferation and differentiation of rBMSCs on the scaffolds

Rat bone marrow stromal cells (rBMSCs) were purchased from the Cell Bank (Chinese Academy of Sciences, Shanghai, China) and maintained in α-MEM medium (GlutaMAX™, Gibco, USA) supplemented with 1% penicillin/streptomycin and 10% fetal bovine serum (FBS). Prior to use, all scaffolds underwent autoclaving to guarantee sterility. For the cell proliferation experiments, rBMSCs at a density of 0.5×10^4 cells per well were seeded onto the scaffolds placed in 48-well plates. These plates were then incubated under a 5% CO$_2$ atmosphere at 37 °C, and cell proliferation was assessed using the CCK-8 assay on days 1, 3 and 7. Furthermore, to visualize cell adhesion and proliferation on the scaffolds, fluorescence staining was performed with a calcein-AM staining kit, and the resulting images were captured using a fluorescence microscope (Zeiss Axio Observer A1, Wetzlar, Germany). The cells were stained with DAPI and phalloidin, and their morphology was subsequently visualized and captured using confocal microscopy.

The migration of rBMSCs was evaluated using a transwell migration assay. The scaffolds were placed in 24-well culture plates for 3 days, and rBMSCs at a density of 5×10^4 cells per well were seeded in the upper chamber. Following 12 hours of incubation, the cells were fixed with 4% paraformaldehyde for 30 minutes and thoroughly washed three times with phosphate buffered saline (PBS). Subsequently, the cells that had migrated to the lower chamber were imaged using a fluorescence microscope (Zeiss Axio Observer A1, Wetzlar, Germany).

To assess the formation of calcium nodules in the rBMSCs, Alizarin Red staining was conducted after 21 days of cell culture. Furthermore, the influence of the scaffolds on osteogenic gene expression in the rBMSCs was evaluated by quanti-

tative real-time reverse transcription polymerase chain reaction (qRT-PCR) after 28 days of cell culture. Total RNA was extracted using Trizol reagent and reverse-transcribed into cDNA. This cDNA was then subjected to polymerase chain reaction (PCR) amplification using a multiplex primer set targeting key osteogenic genes, including osteocalcin (OCN), osteopontin (OPN) and alkaline phosphatase (ALP). PCR primer information of OCN, OPN and ALP is listed in Table S1.†

2.5 Seeding and culturing HUVECs on the scaffolds

Human umbilical vein endothelial cells (HUVECs) were acquired from EK Biosciences (Shanghai, China) and cultivated in an endothelial cell medium (also from EK Biosciences, Shanghai, China) within an incubator maintained at 37 °C under a 5% CO$_2$ atmosphere. To assess cell infiltration in the microchannels, HUVECs were seeded into microchannels of the prepared scaffolds at a density of 1.0×10^4 cells through one open end of the channels and cultured for a period of 7 days. Following cultivation, the cells were stained with DAPI and phalloidin, and their morphology was subsequently visualized and captured using confocal microscopy.

To assess the impact of the scaffolds on angiogenic gene expression in HUVECs, qRT-PCR was performed, adhering to the same protocol as outlined in section 2.3. This analysis targeted the following genes: hypoxia-inducible factor-1 alpha (HIF-1α), vascular endothelial growth factor (VEGF), and platelet endothelial cell adhesion molecule-1 (CD31). PCR primer information for HIF-1α, VEGF and CD31 is listed in Table S1.†

2.6 The evaluation of *in vivo* vascularization of scaffolds in the subcutaneous region

Female Kunming (KM) mice, aged 4–5 weeks, were procured from Guangdong Laboratory Animal Co., Ltd. All animal procedures were performed in accordance with the Guidelines for Care and Use of Laboratory Animals of Shenzhen University and approved by the Animal Ethics Committee of Shenzhen University Health Science Center. Prior to surgery, the mice were anesthetized using isoflurane. Subsequently, sterilized scaffolds (diameter 5 mm), which were pre-treated through autoclaving, were implanted subcutaneously into the mice. After 4 weeks of implantation, the vascularization in the scaffold implanted region was evaluated using micro-computed tomography (μ-CT) analysis. Following the manufacturer's instructions (Flow Tech, Inc., USA), a uniform solution of contrast agent, diluent, and 5% curing agent was prepared and injected into the mice at a rate of 2 mL min^{-1}. The scaffolds and surrounding tissues were then excised from the implant sites. The excised samples were fixed in 4% paraformaldehyde solution before being scanned and reconstructed using μ-CT (μ-CT100, Scanco Medical AG, Switzerland). The resulting images were analyzed to calculate the vascular volume/total tissue volume ratio, providing a quantitative assessment of subcutaneous vascularization induced by the scaffolds.

2.7 The evaluation of *in vivo* bone repair capability of scaffolds

Critical-sized calvarial bone defects in rats were established in accordance with previous research methodologies. Six-week-old female Sprague–Dawley (SD) rats, sourced from Guangdong Laboratory Animal Co., Ltd, were utilized for this experiment. Prior to surgery, the rats were anesthetized using isoflurane administered through a ventilator. Subsequently, cranial defects with a diameter of 5 mm were created, and the prepared scaffolds were implanted into each defect to evaluate their osteogenic potential. All animal procedures were performed in accordance with the Guidelines for Care and Use of Laboratory Animals of Shenzhen University and approved by the Animal Ethics Committee of Shenzhen University Health Science Center. At 4 and 8 weeks post-implantation, the rats were euthanized, and their skulls were subjected to μ-CT imaging. Quantitative analysis encompassed measurements of bone mineral density (BMD), new bone volume relative to tissue volume (BV/TV), and trabecular bone number (Tb.N). For histological and immunohistochemical evaluations, the samples underwent decalcification in 10% EDTA for 4 weeks, followed by paraffin embedding. Sections with a thickness of 4 μm were cut and stained with hematoxylin and eosin (H&E) and Masson's trichrome for histological assessment. Additionally, immunohistochemical staining was performed using primary antibodies directed against OPN, OCN, HIF-1α, and CD31 to further characterize the bone regeneration process and associated vascularization.

2.8 Statistical analysis

All results were obtained from at least three independent experiments in this study and exhibited as mean ± standard deviation using one-way ANOVA analysis. Statistical analysis was carried out using Origin 2022. The statistical significance was defined as $*p < 0.05$.

3 Results and discussion

3.1 Fabrication and characterization of CSH scaffolds

The microstructures of scaffolds hold pivotal roles in governing bone regeneration and vascularization processes.[34] Notably, microchannels have emerged as critical architectural elements, exhibiting profound influences on enhancing bone tissue formation and fostering vascularization.[8–10] However, creating fully interconnected microchannel networks within bioceramic scaffolds that simultaneously encompass precisely controlled macro pores remains a challenge. Co-axial 3D printing is a prevalent technique employed for fabricating microchannels within scaffolds. Nonetheless, the created microchannels often fail to achieve complete interconnectivity, thereby impeding efficient mass exchange and ultimately affecting optimal tissue formation within the scaffolds. Herein, based on our previous study, we developed an effective and facile method to create 3D bioceramic scaffolds with controlled macro pores and fully interconnected microchannels

for vascularized bone repair applications. Firstly, we prepared printing inks consisting of β-TCP powders, alginate and gelatin. Alginate enables surface crosslinking *via* divalent cations, and gelatin enhances the printability of the inks because of its characteristics of temperature sensitivity. Subsequently, 3D scaffolds with meticulously designed macro pores were fabricated *via* extrusion-based 3D printing (Fig. 2a). Afterwards, the printed scaffolds underwent a crucial step involving immersion in a crosslinking solution (such as $CaCl_2$, $CuCl_2$ or $SrCl_2$) for a predetermined duration. This step is pivotal for the formation of CSH scaffolds. During this process, a unique phenomenon occurs: only the surface of the alginate/β-TCP filaments undergoes rapid crosslinking, resulting in dense structures (Fig. 2a). Conversely, the core regions of these filaments remain in an uncrosslinked state due to the crosslinked surface effectively inhibiting the diffusion of crosslinking ions from the periphery towards the center. SEM images and elemental mapping analyses conclusively validated the presence of a dense surface layer coupled with a porous interior within the filaments after crosslinking. Furthermore, the analyses revealed a higher concentration of crosslinking ions (Cu^{2+} and Sr^{2+}) on the surface compared to the interior regions of the filaments, further proving the differential crosslinking patterns (Fig. S1†).

Finally, the uncrosslinked materials residing at the core of the filaments were eliminated, yielding fully interconnected microchannel networks (Fig. S2a and b†). Subsequent to drying and sintering processes, the hollow channeled bioceramic scaffolds exhibited enhanced structural stability and mechanical properties (Fig. 2b and Fig. S2†), although around 15–40% shrinkage occurred (Fig. S2m–o†). The sintering-induced shrinkage process results in a proportional reduction in the overall scaffold dimensions, including pore size, filament diameter, and hollow channel wall thickness, thereby improving the resolution of the printed scaffolds. This phenomenon simultaneously influences two critical scaffold characteristics: (1) porosity declines due to pore coalescence and densification, and (2) mechanical properties are enhanced through microstructural consolidation. Notably, elevated sintering temperatures exacerbate these transformations: higher temperatures promote densification, manifesting as accelerated shrinkage rates, more pronounced porosity reduction, and greater improvement in compressive strength.[35]

Diverse divalent cations (including Ca^{2+}, Sr^{2+}, Cu^{2+}, Zn^{2+}, *etc.*) and Fe^{3+} ions were workable for crosslinking the alginate/β-TCP filaments to produce the fully interconnected microchannels (Fig. S3a†). The wall thickness of the channels could be tuned by the concentration of crosslinking ions and crosslinking time (Fig. 2c and Fig. S3b–d†). As expected, the wall thickness increased as the crosslinking time increased, and a wall thickness as thin as 200 μm could be achieved after crosslinking with 0.1 M Cu^{2+} for 5 min. When the concentration of crosslinking ions was elevated to 0.5 M and the crosslinking duration was extended to 10 minutes, the resulting excessive wall thickness significantly impeded the complete removal of uncrosslinked residues from the core regions of printed fila-
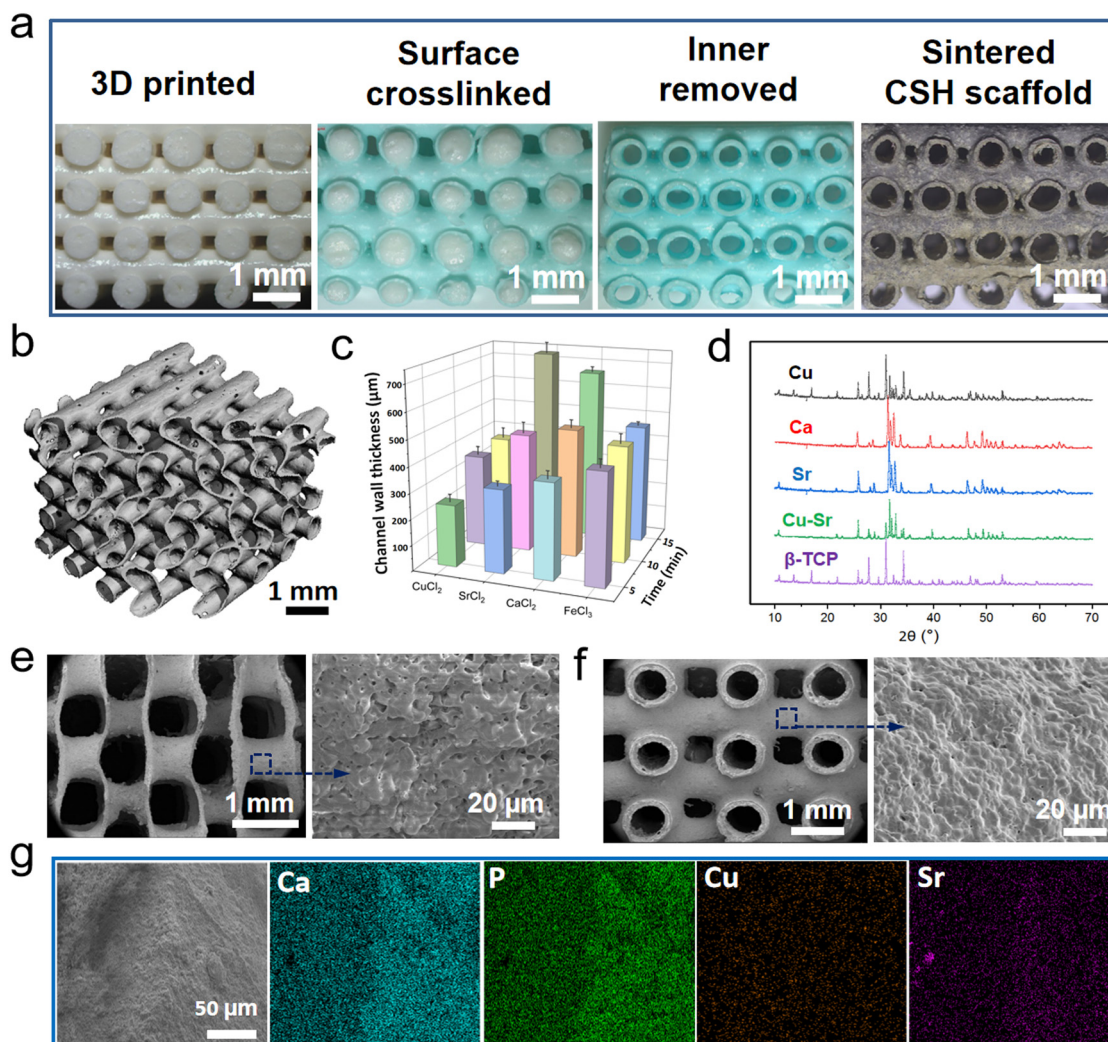
Fig. 2 Fabrication and characterization of the scaffolds. The images showing the process of fabrication of the CSH scaffold: the scaffold after 3D printing, surface crosslinking, removal of inner materials and final sintering (a). The μ-CT image of the prepared CSH scaffold showing the fully interconnected microchannels and macro pores (b), and the effects of different crosslinking agents and time periods (5, 10 and 15 min) on the channel wall thickness of the CSH scaffold (c). XRD patterns of β-TCP scaffold crosslinking using different ions (d). The SEM images of the CSH scaffold on the cross-section and the inner surface of the channel (e), and the longitudinal section and the outer surface of the channel (f). SEM and elemental mapping images of the channel wall (g).

ments. This phenomenon became particularly problematic in delicate architectures, such as thin-diameter filaments and complex 3D scaffold structures, where residual uncrosslinked material entrapment was exacerbated. The morphological evolution induced by these processing parameters ultimately compromised the structural integrity and functional performance of the final fully interconnected hollow channels. Furthermore, bioactive trace elements (such as Sr^{2+}, Cu^{2+}), which are beneficial for osteogenesis and angiogenesis, could be introduced in the bioceramic scaffolds during crosslinking. XRD analysis revealed a similar pattern across all samples, irrespective of the incorporation of various trace elements into the β-TCP scaffolds (Fig. 2d). This observation indicated that the doping of bioactive elements *via* this methodology did not significantly alter the β-TCP phase. The CSH scaffolds were

further characterized by SEM and elemental mapping. The SEM images captured on both the cross-section and vertical section of the CSH scaffold vividly demonstrated the complete interconnectivity of the microchannels between distinct layers (Fig. 2e and f). This interconnected microchannel network, which was unattainable in channeled scaffolds produced by coaxial 3D printing (CSC scaffold),[19] underscores the unique structural advantages of the CSH scaffolds. Additionally, SEM images also showed the perfectly tubular shape of the channels within the CSH scaffold, suggesting that even in thick scaffolds, the microchannels maintained their standard tubular morphology without any distortion (Fig. 2f). In contrast, the microchannels of bioceramic scaffolds fabricated by coaxial 3D printing often succumb to deformation, primarily attributed to the influence of gravity.[19] High-magnification

SEM images revealed that the outer surface of hollow channels exhibited a denser microstructure than the inner surface (Fig. 2e and f). Further elemental mapping analysis confirmed the uniform distribution of the dopant elements, Cu and Sr, throughout the CSH scaffold (Fig. 2g). Notably, EDS analysis yielded weight percentages of 1.75% for Cu and 3.31% for Sr in the CSH scaffold, slightly surpassing their respective concentrations in the CSS scaffold (Fig. S4†).
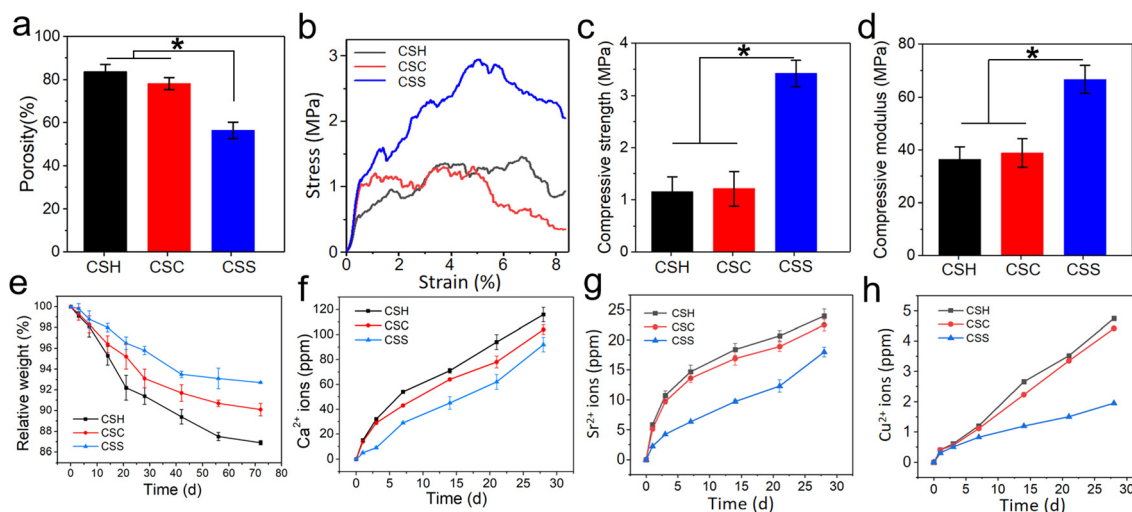
3.2 Mechanical properties and degradation of the prepared bioceramic scaffolds

The total porosity of the scaffold was measured and the data showed that the porosity of the CSH scaffold was 83.6 ± 3.4%, which was significantly higher than that of the CSS scaffold (56.5 ± 3.8%) (Fig. 3a). This notable increase in porosity, approximately 27%, can be attributed to the presence of the microchannels within the CSH scaffold. Furthermore, the porosity of CSH was slightly greater than that of CSC (78.2 ± 2.8%), suggesting that full interconnection among channels may also contribute to an elevation in porosity. The mechanical properties of the prepared bioceramic scaffolds were measured, including the compressive strength and modulus. The data revealed that CSH scaffolds exhibited a compressive strength of 1.15 ± 0.29 MPa and a modulus of 36.41 ± 4.67 MPa. These values did not demonstrate a significant difference when compared to those for CSC scaffolds. However, they were notably lower than the compressive strength and modulus of CSS scaffolds, which were 3.42 ± 0.25 MPa and 66.72 ± 5.23 MPa, respectively (Fig. 3b–d and Table 1). Apparently, the fully interconnected microchannels within the CSH scaffold resulted in a substantial elevation in total porosity, which then caused the loss of some mechanical properties. It is well known that the mechanical properties of the bioceramic scaffolds are related to many parameters, such as the porosity and pore structure.[36,37] Typically, a notable inverse correlation is observed between mechanical properties and porosity, wherein an increase in porosity tends to coincide with a deterioration in mechanical properties.[38] This underscores the inherent challenge in optimizing both attributes simultaneously in the design of bone scaffolds. Meanwhile, the pore architecture assumes a pivotal role in affecting the mechanical properties of porous scaffolds.[39] Previous studies have demonstrated that an ordered pore structure can impart higher mechanical properties to porous scaffolds, as compared to those featuring a random pore arrangement.[40,41] Furthermore, for β-TCP scaffolds, the sintering process plays a crucial role in modulating their mechanical properties. By optimizing the sintering efficiency, it is possible to achieve scaffolds with tailored mechanical characteristics, thereby enhancing their performance and suitability for specific applications.[42] In the present study, although the compressive strength of CSH was insufficient for adapting load-bearing bone defects directly, it was sufficient for handling and suitable for *in vitro* and in *in vivo* experiments.

The *in vitro* degradation of the scaffold was assessed through a 70-day incubation period in PBS. The results indicated that all scaffolds exhibited a limited degradation rate within this environment, evidenced by the CSH scaffold undergoing a weight loss of approximately 13% after 70 days of incubation (Fig. 3e). Anyway, from day 14 onward, the degradation rate of the CSH scaffold exceeded that of the CSS scaffold, indicating that the presence of microchannels significantly enhanced the degradation process. Furthermore, over the entire 70-day incubation period, the CSH scaffold demonstrated a greater weight loss compared to the CSC scaffold, suggesting that the fully interconnected microchannel network plays a critical role in accelerating degradation. This is likely because the full interconnection facilitates enhanced mass exchange and liquid perfusion.

Additionally, the release of calcium, copper and strontium ions from the scaffolds during 28 days of incubation was meti-

Fig. 3 The mechanical properties and *in vitro* degradation. The porosity (a), stress–strain curves (b), compressive strength (c) and modulus (d) of CSH, CSC and CSS scaffolds. The relative weight of the three types of scaffolds during 70 days of *in vitro* degradation (e), and the release of calcium (f), strontium (g) and copper (h) ions from the scaffolds during 28 days of incubation *in vitro*.

culously monitored. According to the received data (Fig. 3f–h), the three types of ions showed sustained release during the incubation period, and no apparent initial burst release was observed for all scaffolds, which could avoid the concentration-dependent cytotoxicity of copper and strontium ions. In comparison with the CSS scaffold, the CSH scaffold exhibited faster and greater release of ions. This enhanced release is evidently attributable to the increased surface areas and porosity facilitated by the microchannels in the CSH scaffold. The release kinetics of ions are linked to the degradation of 3D-printed β-TCP scaffolds. Consequently, the factors influencing the degradation of these scaffolds serve as regulators of ion release. Key factors are the scaffolds' porosity and specific surface area, the grain size and crystal configuration of the β-TCP material, and environmental conditions such as pH value, temperature, ionic strength, and the presence of coexisting ions in the surrounding solution.[43] In the *in vivo* setting, the release kinetics of ions is further shaped by dynamic interactions between the scaffold materials and the surrounding tissues.

3.3 Cell (rBMSCs and HUVECs) culture on the bioceramic scaffolds

To assess the cytocompatibility of CSC, CSS and CSH scaffolds, live cell assays and CCK-8 assays were conducted following the seeding and culturing of rBMSCs on the respective scaffolds

for a period of 7 days. From the fluorescence images, rBMSCs showed high viability on all three types of scaffolds over the culturing time (Fig. 4a). With the culturing time extending, the cell density on the scaffolds significantly increased. After a 7-day culture period, the entire surfaces of all scaffolds were nearly fully covered by cells with a well-spread morphology. Notably, all scaffolds supported good cell proliferation throughout the 7 days of culturing. In particular, cells on CSH scaffolds exhibited superior growth activity compared to those on CSS scaffolds (Fig. 4b), which might be attributed to the improved delivery of oxygen and nutrients facilitated by the interconnected hollow channel networks within the CSH scaffold, along with the beneficial effects of ions released from the scaffold.[44]

In addition, when seeded from the open ends of the channels, HUVECs not only adhered effectively but also flourished on the inner surfaces of these hollow structures (Fig. 4c). HUVECs can be efficiently seeded within the fully interconnected channels *via* injection through one open channel. Cells could migrate and infiltrate into the interconnected hollow channels of the CSH scaffold during *in vitro* culture and *in vivo* implantation (Fig. 4d). Furthermore, these cells exhibited robust adhesion to the interior surfaces of the channels. Upon seven days of culturing, examination using fluorescence and confocal laser microscopy, facilitated by cutting through the hollow channels, revealed that the cells had proliferated favor-
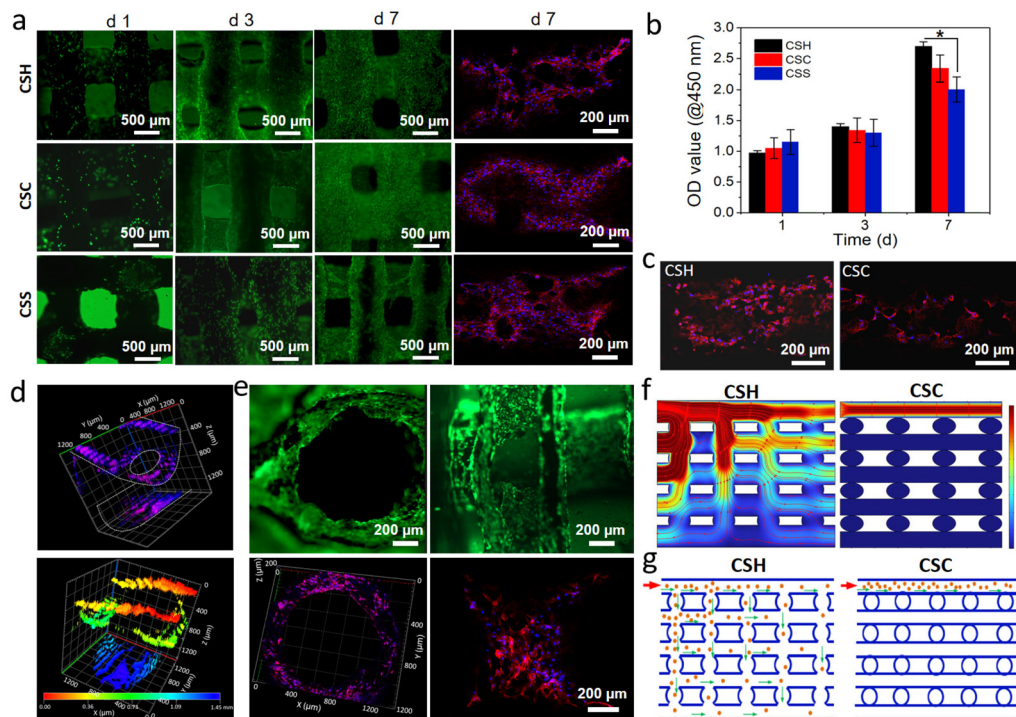
Fig. 4 Biocompatibility and cell infiltration of scaffolds. The fluorescence microscopy and confocal laser microscopy images (a) and proliferation (b) of rBMSCs on CSH, CSC and CSS scaffolds after 1, 3 and 7 days of culture. The confocal laser microscopy images of HUVECs cultured in the channels of CSH and CSC scaffolds for 7 days (c). The fluorescence microscopy and confocal laser microscopy images of HUVECs in the microchannels of the CSH scaffold after seeding through one open end of the filament (d and e). Simulation (f) and schematic illustrating (g) the possible infiltration route of cells from one open end of channels to the center of the CSH and CSC scaffolds.

ably within these spaces, attaining an initial state of endothelialization (Fig. 4e). In comparison, the channels within the CSC scaffold, created through coaxial 3D printing, lacked interconnectivity, making it challenging for cells and substances within one channel to migrate and transfer to others. Conversely, the CSH scaffold boasted a distinct advantage: its fully interconnected network of microchannels. This feature not only enabled efficient cell seeding within the channels by injecting cells through a single open end but also facilitated mass exchange and cell infiltration throughout the interconnected channels (Fig. 4f and g). Consequently, the CSH scaffold, distinguished by its excellent cytocompatibility, presents itself as an ideal platform for spatially co-culturing BMSCs and HUVECs. This can be achieved by positioning BMSCs on the exterior and strategically seeding HUVECs within the fully interconnected channel network of the scaffolds.

3.4　*In vitro* cell migration

The migration of host stem cells to the defect areas is pivotal for successful bone repair.[45,46] During bone repair, mesenchymal stem cells mobilized from the bone marrow were recruited to the defect site and then differentiated into osteoblasts for effective bone regeneration.[47] Therefore, the implantation of porous scaffolds designed to enhance mesenchymal stem cell recruitment holds significant potential in accelerating bone repair.[48] Herein, the ability of the scaffold to recruit rBMSCs was assessed using an *in vitro* transwell migration assay. According to the received data, compared with the CSS scaffold, significantly more cells were induced by the CSH scaffold to penetrate the transwell membranes (Fig. 5a and c). Apparently, the released ions from scaffolds play an important role in cell migration, especially the Sr^{2+} ions. It has been demonstrated that Sr^{2+} ions could activate the deposition of fibronectin,[49] which is an important extracellular matrix protein for cell proliferation and migration. Furthermore, by incorporating fully interconnected microchannels, the CSH scaffold offers a dependable system for enhancing cell migration, particularly for cells transitioning from peripheral regions to the center of the scaffold.[50]

### 3.5　*In vitro* osteogenesis and angiogenesis evaluation

The *in vitro* osteogenic potential of the scaffolds was assessed through both quantitative and qualitative analyses of mineral deposition, employing Alizarin Red S staining. Following 21 days of culturing, Alizarin Red S staining was applied to each sample. Visual inspection of both digital and microscopic images revealed discernible mineral deposition across all three groups (Fig. 5b). Nevertheless, a closer examination of the images and subsequent quantitative analysis demonstrated the superior performance of the CSH scaffold, with significantly more mineral nodules formed compared to the CSS group (Fig. 5d). This finding indicated the enhanced osteogenic effect imparted by the CSH scaffold. In addition, the expression of osteogenic differentiation related genes including OCN, ALP and OPN was also measured by qRT-PCR after

culturing rBMSCs on the scaffolds for 28 days. As shown in Fig. 5e–g, OCN, ALP and OPN were all significantly up-regulated in the CSH scaffold. Furthermore, after culturing HUVECs on the scaffolds for 28 days, the expression levels of angiogenesis-associated genes, including HIF-1α, CD31, and VEGF, were observed to be markedly elevated in the CSH group, showing the highest expression levels among all of the groups (Fig. 5h–j).

3.6　*In vivo* vascularization and bone repair assessment

Vascularization plays a pivotal role in fostering bone tissue regeneration during the bone repair process.[51,52] Herein, to evaluate the ability of the prepared scaffolds to stimulate vascularization *in vivo*, they were implanted into the subcutaneous area of mice. Following a four-week implantation period, the specimens were harvested and subjected to 3D reconstructed µ-CT imaging. The resulting images (Fig. 6a) revealed a significantly higher density of vessels within the CSH scaffold compared to the other three groups, underscoring its enhanced capacity to induce vascularization. In particular, several newly formed vessels were observed to penetrate the entire CSH scaffold, indicating the remarkable ability to facilitate vessel formation even within the core region of the scaffold. Quantitative analysis confirmed that the relative vessel volume within the CSH scaffold was significantly elevated compared to CSC and CSS scaffolds (Fig. 6b). Additionally, from the µ-CT images, most of the vessels were observed in the peripheral area of the CSS and CSC scaffolds, while few vessels were in the center of the scaffold. These observations underscore that the fully interconnected hollow channels in the CSH scaffold play a pivotal role in accelerating *in vivo* vascularization, particularly by enhancing the formation of new vessels within the interior of the 3D scaffold. However, it is crucial to acknowledge that this process is likely to be synergistically facilitated by the presence of bioactive ions,[20] which contribute to creating an optimal environment for vessel growth and tissue regeneration.

The *in vivo* bone repair efficacy of the fabricated scaffolds was assessed through their implantation into rat calvarial defects for durations of 4 and 8 weeks. Following this period, the samples were harvested for comprehensive analysis using µ-CT scanning, histological staining and immunohistochemical staining. The 3D-reconstructed µ-CT images revealed that, at 4 weeks after implantation, a notably greater amount of hard tissue was evident within the CSH scaffold compared to the other groups (Fig. 6c). Furthermore, the CSH scaffold demonstrated good osseointegration, characterized by a seamless interface between the scaffold and host bone tissues, whereas discernible gaps were apparent at the scaffold–bone interface in the other three groups. After an 8-week implantation period (Fig. 6d), the defect areas in all groups had significantly diminished, approaching the original boundaries. Notably, all scaffolds exhibited remarkable osseointegration with the host bone. In particular, the CSH group demonstrated a superior outcome, with a more abundant generation of newly formed bone tissues leading to complete healing of the
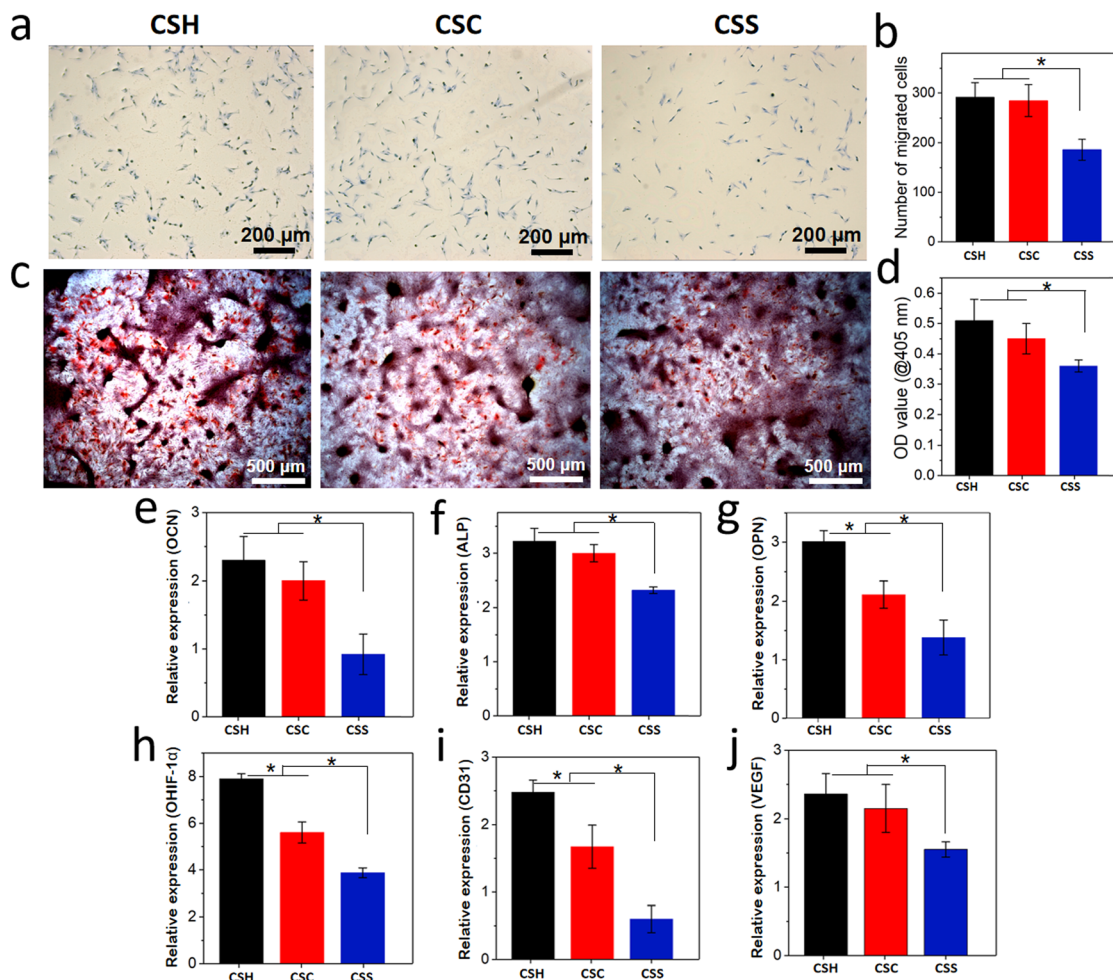
Fig. 5 *In vitro* evaluation of the cell migration, angiogenic and osteogenic ability of scaffolds. Cell migration study using the transwell method by co-culturing rBMSCs with CSH, CSC and CSS scaffolds, respectively (a and b). The microscopic images (c) and quantitative analysis (d) of Alizarin Red S staining of BMSCs cultured with extracts from different scaffolds. Osteogenic gene expression of BMSCs cultured on 3D printed scaffolds, including OCN (e), ALP (f) and OPN (g). Angiogenic gene expression of HUVECs cultured on 3D printed scaffolds, including HIF-1α (h), CD31 (i) and VEGF (j).

defect. In contrast, the untreated control group continued to exhibit substantial bone defect areas at both 4 and 8 weeks, serving as a stark reminder of the importance of intervention. Furthermore, a quantitative analysis of BMD, BV/TV, and Tb.N within the region of interest was conducted based on the reconstructed μ-CT images. The results indicated a substantial elevation in BMD, BV/TV, and Tb.N in the CSH group compared to the CSS and control groups at both 4 and 8 weeks post-implantation. Furthermore, at 8 weeks, the CSH group surpassed all the other four groups in these parameters, which further suggested that the implantation of CSH scaffolds facilitated significantly more new bone tissue formation within the defect site than the other treatments (Fig. 6e–g).

To further validate the bone regenerative potential of the scaffolds, H&E staining, Masson's trichrome staining, and immunofluorescence analysis were conducted. At 4 weeks post-implantation (Fig. 7a and b), H&E staining and Masson's trichrome staining images revealed minimal new bone for-

mation in the central region of the defect across all groups. However, in the CSH group, notable new bone tissues were discernible along the periphery of the defect, indicating a superior bone repair capability of the CSH scaffolds. At 8 weeks (Fig. 7c and d), although new bone tissues were discernible in the vicinity of the scaffolds in the CSS and CSC groups, the central defect region remained largely occupied by the scaffolds and fibrous tissues, with minimal bone formation. Conversely, the CSH group demonstrated a remarkable increase in new bone formation, not merely confined to the perimeter of the defect but also profusely within the hollow channels of the CSH scaffold, underscoring its exceptional capacity for bone regeneration (Fig. 7c, d and Fig. S5†). Specifically, all scaffold-implanted groups demonstrated the growth of new blood vessels. Notably, the CSH scaffold stood out, exhibiting a significantly higher density of vessels both externally (Fig. 7e) and internally (Fig. 7f) within the hollow channels, in comparison with the other groups.
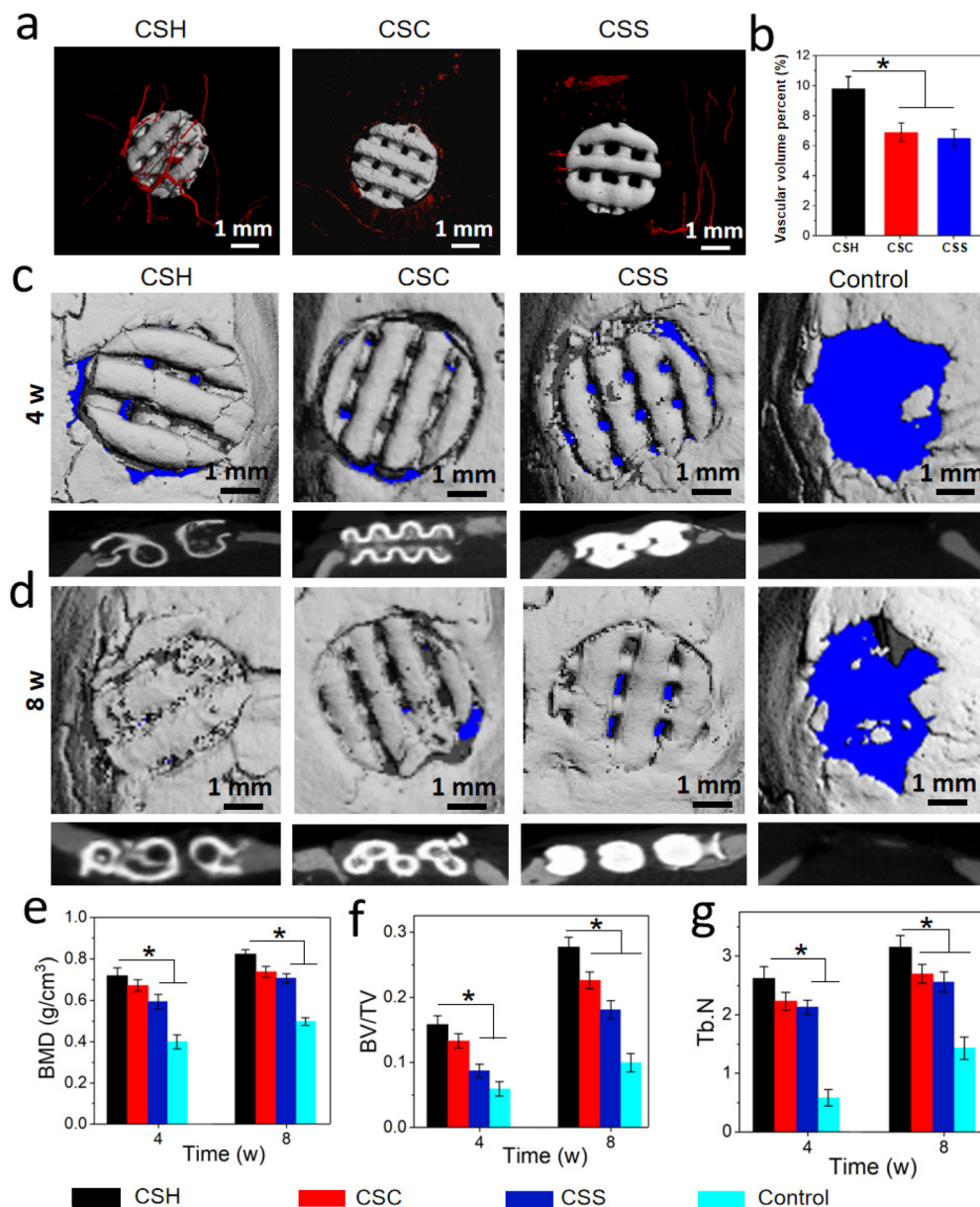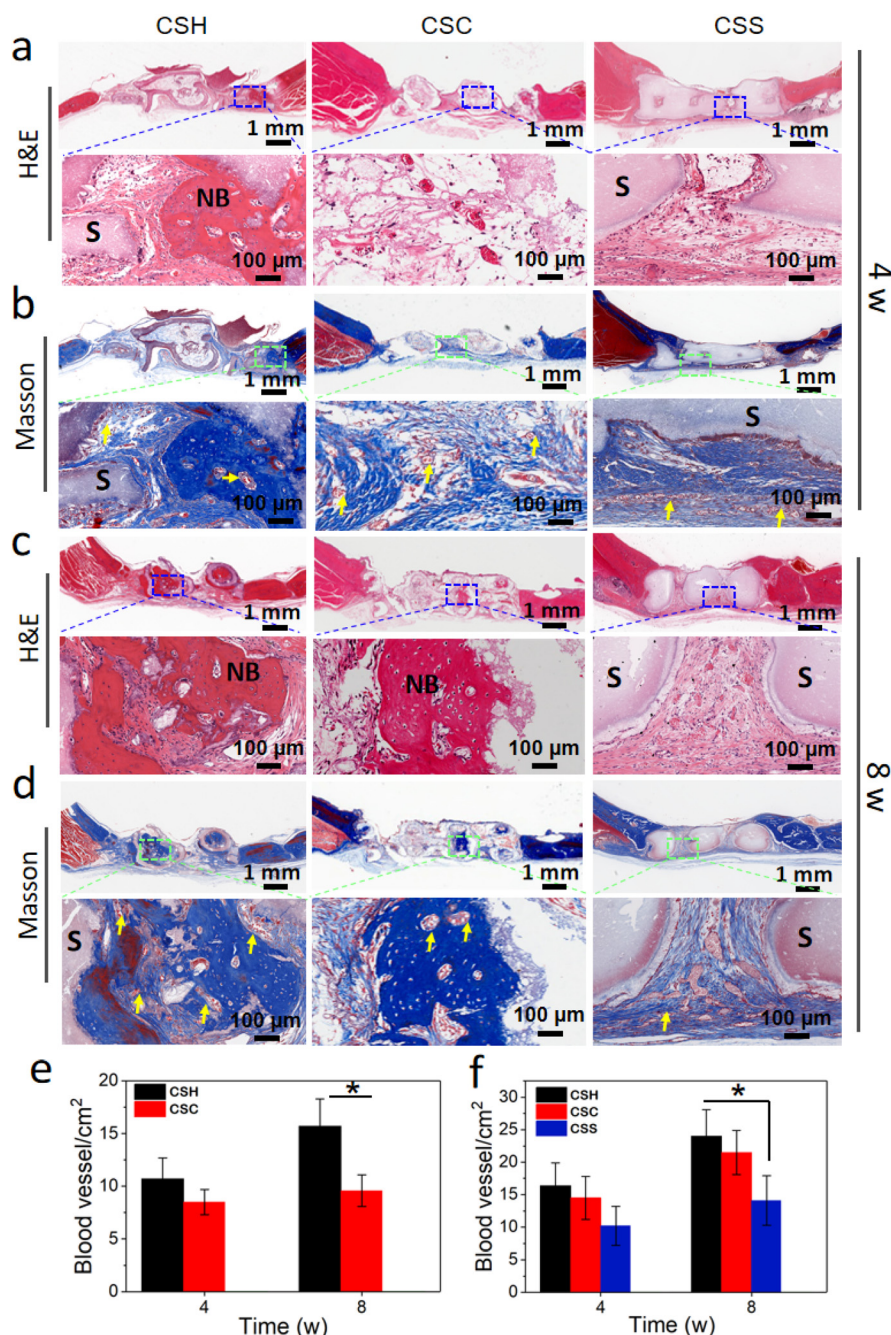
Fig. 6 *In vivo* evaluation of vascularization and bone repair of scaffolds. The μ-CT images (a) and quantitative analysis (b) of neovascularization after subcutaneous implantation of different scaffolds for 4 weeks. 3D reconstruction of micro-CT images and section view of new bone formation in defect areas after different treatments for 4 (c) and 8 (d) weeks. Bone mineral density (BMD) (e), bone volume/tissue volume (BV/TV) (f) and trabecular bone number (Tb.N) (g) of regenerated bone in the region of interest.

Previous studies demonstrated that copper can promote angiogenesis by stabilizing and regulating the expression of HIF-1α.[53–55] Then, immunofluorescence staining of HIF-1α was performed to confirm the activation of the HIF-1α pathway after scaffold implantation for 8 weeks. From the results (Fig. 8a–c), the fluorescence signal of HIF-1α in the CSH group was higher than that in the other groups, suggesting that the CSH scaffold can enhance angiogenesis in skull defects by activating the HIF-1α pathway. Additionally, CD31, as an important component of angiogenesis,[56] showed an increased expression in the CSH group. Augmented CD31 expression

facilitated the adhesion and aggregation of HUVECs, promoted angiogenesis, and supplied essential nutrients and oxygen to the newly formed bone tissue.[57,58] Immunofluorescence staining for OCN and OPN was also performed on the newly formed bone tissue in all groups. As shown in Fig. 8d and e, the sample treated with the CSH scaffold showed higher OCN and OPN expression, compared with the samples treated with CSC and CSS scaffolds, which was consistent with the results of histological staining.

Thus, the architectural features of bone scaffolds are pivotal determinants that influence their *in vivo* performance in bone

Fig. 7 Evaluation of the vascularization and bone formation by H&E and Masson's trichrome staining. The staining images of the bone defect area after treatment by different scaffolds for 4 (a and b) and 8 (c and d) weeks, and the vessel numbers in the inside (e) and outside (f) of the microchannels of scaffolds. NB: new bone; S: scaffold; yellow arrows denote vessels.

regeneration. Optimizing the scaffold architectures represents one of the most cost-effective and efficient strategies to boost bone repair outcomes. In this study, we demonstrated that fully interconnected hollow channels significantly enhanced vascularization and bone formation in rat skull defects. This enhancement was attributed not only to the improved mass exchange facilitated by the fully interconnected hollow channels but also to their ability to promote cell proliferation,

migration, and differentiation, probably by activating the mitogen-activated protein kinase (MAPK) pathway.[27] Furthermore, the CSH scaffolds demonstrate the potential for synergistic integration with advanced therapeutic modalities to further enhance osteoregenerative efficacy. A compelling example involves surface modification of the scaffold with bioactive photothermal agents, enabling precise modulation of the local osseous microenvironment. This strategic combi-
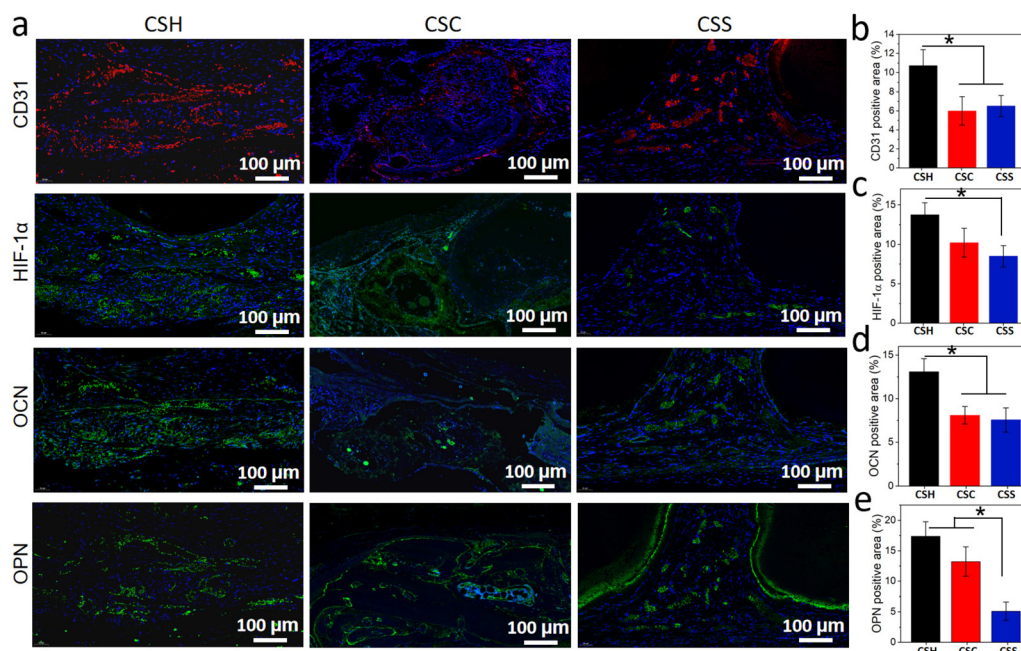
Fig. 8 Evaluation of the vascularization and bone formation by immunofluorescence staining. Immunofluorescence staining of CD31 (red), HIF-1α (green), OCN (green) and OPN (green) after scaffolds implantation for 8 weeks (a). The cell nuclei were stained with DAPI (blue). Quantitative analysis of CD31 (b), HIF-1α (c), OCN (d) and OPN (e) expression positive areas using Image J software.

nation leverages mild photothermal therapy to induce controlled hyperthermic stimuli, which synergistically promotes osteogenic differentiation of mesenchymal stem cells, upregulates angiogenic factor expression, and enhances extracellular matrix mineralization.[59–62] Moreover, drugs and growth factors can be incorporated into the hollow channels to further augment the *in vivo* efficacy of the scaffolds. This approach not only enhances their capacity to promote vascularization and bone regeneration but also endows them with additional capabilities, such as serving as a therapeutic platform for inhibiting postsurgical bone tumor recurrence and metastasis.[63,64] Although the *in vivo* data demonstrated that the CSH scaffold promoted vascularized bone regeneration primarily by introducing fully interconnected hollow channels, it should be noted that its mechanical properties remain suboptimal for real applications. Future studies could involve post-treatment modifications to enhance the mechanical strength of the CSH scaffold. Additionally, creating critical-size bone defects in large animal models would enable a systematic evaluation of the bone regenerative capacity, which is essential for translating the scaffolds into clinical applications in the future.

4   Conclusion

In summary, β-TCP based bioceramic scaffolds with both macro pores and fully interconnected hollow channels were successfully fabricated by using 3D printing and surface crosslinking. Meanwhile, bioactive ions including copper and strontium ions can be selectively introduced in the hollow β-TCP

scaffolds (CSH) during surface crosslinking. The CSH scaffolds with high porosity showed enhanced structural integrity after sintering. Furthermore, the fully interconnected hollow channels in CSH scaffolds accelerated material degradation and bioactive ion release. *In vitro* experiments showed enhanced effects of CSH scaffolds on promoting angiogenesis and osteogenesis. An *in vivo* study further confirmed that the skull defect in rats was almost completely healed following an 8-week implantation period with the CSH scaffolds. Notably, new bone tissues and blood vessels formed not only on the exterior but also extensively within the interconnected hollow channels of the CSH scaffolds. These findings highlight the significant role of the fully interconnected hollow channel architecture in enhancing vascularized bone repair.

Conflicts of interest

There are no conflicts to declare.

Abbreviations

ALP	Alkaline phosphatase
β-TCP	β-Tricalcium phosphate
BMD	Bone mineral density
BV/TV	New bone volume relative to tissue volume
CD31	Platelet endothelial cell adhesion molecule-1
CSH	The copper/strontium ion doped β-TCP scaffolds with fully interconnected hollow channels

CSC	The copper/strontium ion doped β-TCP scaffold with non-interconnected hollow channels *via* co-axial printing
CSS	The copper/strontium ion doped β-TCP scaffolds with solid filaments (without hollow channels).
DAPI	4′,6-Diamidino-2-phenylindole
EDS	Energy dispersive X-ray spectroscopy
HIF-1α	Hypoxia-inducible factor-1 alpha
HUVECs	Human umbilical vein endothelial cells
μ-CT	Micro-computed tomography
OCN	Osteocalcin
OPN	Osteopontin
PBS	Phosphate buffered saline
rBMSCs	Rat bone marrow stromal cells
SEM	Scanning electron microscopy
Tb.N	Trabecular bone number
VEGF	Vascular endothelial growth factor
XRD	X-Ray diffractometry

Data availability

All relevant data supporting the findings of this research are available from the corresponding author upon reasonable request.

Acknowledgements

References

1 M. N. Collins, G. Ren, K. Young, S. Pina, R. L. Reis and J. M. Oliveira, Scaffold fabrication technologies and structure/function properties in bone tissue engineering, *Adv. Funct. Mater.*, 2021, **31**, 2010609.

2 K. F. Eichholz, F. E. Freeman, P. Pitacco, J. Nulty, D. Ahern, R. Burdis, D. C. Browe, O. Garcia, D. A. Hoey and D. J. Kelly, Scaffold microarchitecture regulates angiogenesis and the regeneration of large bone defects, *Biofabrication*, 2022, **14**, 045013.

3 D. Pierantozzi, A. Scalzone, S. Jindal, L. Stīpniece, K. Šalma-Ancāne, K. Dalgarno, P. Gentile and E. Mancuso, 3D printed Sr-containing composite scaffolds: Effect of structural design and material formulation towards new strategies for bone tissue engineering, *Compos. Sci. Technol.*, 2020, **191**, 108069.

4 Y. Li, Y. Xiao and C. Liu, The horizon of materiobiology: A perspective on material-guided cell behaviors and tissue engineering, *Chem. Rev.*, 2017, **117**, 4376–4421.

5 X. Liu, Y. Miao, H. Liang, J. Diao, L. Hao, Z. Shi, N. Zhao and Y. Wang, 3D-printed bioactive ceramic scaffolds with biomimetic micro/nano-HAp surfaces mediated cell fate and promoted bone augmentation of the bone–implant interface *in vivo*, *Bioact. Mater.*, 2022, **12**, 120–132.

6 L. Bai, P. Chen, Y. Zhao, R. Hang, X. Yao, B. Tang, C. Liu, Y. Xiao and R. Hang, A micro/nano-biomimetic coating on titanium orchestrates osteo/angio-genesis and osteoimmunomodulation for advanced osseointegration, *Biomaterials*, 2021, **278**, 121162.

7 H. Mohammadi, M. Sepantafar, N. Muhamad and A. B. Sulong, How does scaffold porosity conduct bone tissue regeneration?, *Adv. Eng. Mater.*, 2021, **23**, 2100463.

8 Y. Luo, B. Chen, X. Zhang, S. Huang and Q. Wa, 3D printed concentrated alginate/GelMA hollow-fibers-packed scaffolds with nano apatite coatings for bone tissue engineering, *Int. J. Biol. Macromol.*, 2022, **202**, 366–374.

9 X. Wang, Y. Yu, C. Yang, C. Shao, K. Shi, L. Shang, F. Ye and Y. Zhao, Microfluidic 3D printing responsive scaffolds with biomimetic enrichment channels for bone regeneration, *Adv. Funct. Mater.*, 2021, **31**, 2105190.

10 J. Yang, Z. Chen, C. Gao, J. Liu, K. Liu, X. Wang, X. Pan, G. Wang, H. Sang, H. Pan, W. Liu and C. Ruan, A mechanical-assisted post-bioprinting strategy for challenging bone defects repair, *Nat. Commun.*, 2024, **15**, 3565.

11 K. S. Lim, M. Baptista, S. Moon, T. B. Woodfield and J. Rnjak-Kovacina, Microchannels in development, survival, and vascularisation of tissue analogues for regenerative medicine, *Trends Biotechnol.*, 2019, **37**, 1189–1201.

12 Y. Kang and J. Chang, Channels in a porous scaffold: A new player for vascularization, *Regener. Med.*, 2018, **13**, 705–715.

13 J. Rnjak-Kovacina, L. S. Wray, J. M. Golinski and D. L. Kaplan, Arrayed hollow channels in silk-based scaffolds provide functional outcomes for engineering critically sized tissue constructs, *Adv. Funct. Mater.*, 2014, **24**, 2188–2196.

14 X. Yuan, W. Zhu, Z. Yang, N. He, F. Chen, X. Han and K. Zhou, Recent advances in 3D printing of smart scaffolds for bone tissue engineering and regeneration, *Adv. Mater.*, 2024, **36**, 2403641.

15 M. Mirkhalaf, Y. Men, R. Wang, Y. No and H. Zreiqat, Personalized 3D printed bone scaffolds: A review, *Acta Biomater.*, 2023, **156**, 110–124.

16 C. Dong, H. Wei, X. Zhang, Y. Li, L. Huang, Q. Wa and Y. Luo, 3D printed hydrogel/wesselsite-PCL composite scaffold with structural change from core/shell fibers to microchannels for enhanced bone regeneration, *Composites, Part B*, 2022, **246**, 110264.

17 A. Entezari, Q. Wu, M. Mirkhalaf, Z. Lu, I. Roohani, Q. Li, C. R. Dunstan, X. Jiang and H. Zreiqat, Unraveling the influence of channel size and shape in 3D printed ceramic scaffolds on osteogenesis, *Acta Biomater.*, 2024, **180**, 115–127.

18 L. Shao, Q. Gao, C. Xie, J. Fu, M. Xiang and Y. He, Directly coaxial 3D bioprinting of large-scale vascularized tissue constructs, *Biofabrication*, 2020, **12**, 035014.

19 Y. Luo, D. Zhai, Z. Huan, H. Zhu, L. Xia, J. Chang and C. Wu, Three-dimensional printing of hollow-struts-packed bioceramic scaffolds for bone regeneration, *ACS Appl. Mater. Interfaces*, 2015, **7**, 24377–24383.

20 W. Zhang, C. Feng, G. Yang, G. Li, X. Ding, S. Wang, Y. Dou, Z. Zhang, J. Chang, C. Wu and X. Jiang, 3D-printed scaffolds with synergistic effect of hollow-pipe structure and bioactive ions for vascularized bone regeneration, *Biomaterials*, 2017, **135**, 85–95.

21 J. Li, H. Huang, T. Xu, J. Li, T. Guo, X. Lu, J. Ren, X. Ren, Y. Mu and J. Weng, Effect of the interconnecting window diameter of hydroxyapatite scaffolds on vascularization and osteoinduction, *Ceram. Int.*, 2022, **48**, 25070–25078.

22 R. Wu, Y. Li, M. Shen, X. Yang, L. Zhang, X. Ke, G. Yang, C. Gao, Z. Gou and S. Xu, Bone tissue regeneration: the role of finely tuned pore architecture of bioactive scaffolds before clinical translation, *Bioact. Mater.*, 2021, **6**, 1242–1254.

23 D. B. Kolesky, K. A. Homan, M. A. Skylar-Scott and J. A. Lewis, Three-dimensional bioprinting of thick vascularized tissues, *Proc. Natl. Acad. Sci. U. S. A.*, 2016, **113**, 3179–3184.

24 R. Xie, W. Zheng, L. Guan, Y. Ai and Q. Liang, Engineering of hydrogel materials with perfusable microchannels for building vascularized tissues, *Small*, 2020, **16**, 1902838.

25 M. Ryma, H. Genç, A. Nadernezhad, I. Paulus, D. Schneidereit, O. Friedrich, K. Andelovic, S. Lyer, C. Alexiou, I. Cicha and J. Groll, A print-and-fuse strategy for sacrificial filaments enables biomimetically structured perfusable microvascular networks with functional endothelium inside 3D hydrogels, *Adv. Mater.*, 2022, **34**, 2200653.

26 Y. Luo, T. Zhang and X. Lin, 3D printed hydrogel scaffolds with macro pores and interconnected microchannel networks for tissue engineering vascularization, *Chem. Eng. J.*, 2022, **430**, 132926.

27 T. Wang, M. Zhang, J. Guo, H. Wei, W. Li and Y. Luo, Alginate/bacterial cellulose/GelMA scaffolds with aligned nanopatterns and hollow channel networks for vascularized bone repair, *Int. J. Biol. Macromol.*, 2025, **308**, 142578.

28 E. Zeimaran, S. Pourshahrestani, A. Fathi, N. A. Abd Razak, N. A. Kadri, A. Sheikhi and F. Baino, Advances in bioactive glass-containing injectable hydrogel biomaterials for tissue regeneration, *Acta Biomater.*, 2021, **136**, 1–36.

29 C. Lei, J. Song, S. Li, Y. Zhu, M. Liu, M. Wan, Z. Mu, F. R. Tay and L. Niu, Advances in materials-based therapeutic strategies against osteoporosis, *Biomaterials*, 2023, **296**, 122066.

30 C. Zhao, W. Liu, M. Zhu, C. Wu and Y. Zhu, Bioceramic-based scaffolds with antibacterial function for bone tissue engineering: A review, *Bioact. Mater.*, 2022, **18**, 383–398.

31 M. Zhang, R. Lin, X. Wang, J. Xue, C. Deng, C. Feng, H. Zhuang, J. Ma, C. Qin, L. Wan, J. Chang and C. Wu, 3D printing of Haversian bone-mimicking scaffolds for multi-cellular delivery in bone regeneration, *Sci. Adv.*, 2020, **6**, eaaz6725.

32 W. Zhi, X. Wang, D. Sun, T. Chen, B. Yuan, X. Li, X. Chen, J. Wang, Z. Xie, X. Zhu, K. Zhang and X. Zhang, Optimal regenerative repair of large segmental bone defect in a goat model with osteoinductive calcium phosphate bioceramic implants, *Bioact. Mater.*, 2022, **11**, 240–253.

33 M. Duan, S. Ma, C. Song, J. Li and M. Qian, Three-dimensional printing of a β-tricalcium phosphate scaffold with dual bioactivities for bone repair, *Ceram. Int.*, 2021, **47**, 4775–4782.

34 J. Ma, Y. Li, Y. Mi, Q. Gong, P. Zhang, B. Meng, J. Wang, J. Wang and Y. Fan, Novel 3D printed TPMS scaffolds: Microstructure, characteristics and applications in bone regeneration, *J. Tissue Eng.*, 2024, **15**, 20417314241263689.

35 L. Kaewsichan, D. Riyapan, P. Prommajan and J. Kaewsrichan, Effects of sintering temperatures on micromorphology, mechanical properties, and bioactivity of bone scaffolds containing calcium silicate, *Sci. Asia*, 2011, **37**, 240–246.

36 H. Jodati, B. Yılmaz and Z. Evis, A review of bioceramic porous scaffolds for hard tissue applications: Effects of structural features, *Ceram. Int.*, 2020, **46**, 15725–15739.

37 F. Darus, R. M. Isa, N. Mamat and M. Jaafar, Techniques for fabrication and construction of three-dimensional bioceramic scaffolds: Effect on pores size, porosity and compressive strength, *Ceram. Int.*, 2018, **44**, 18400–18407.

38 Z. Miri, H. J. Haugen, D. Loca, F. Rossi, G. Perale, A. Moghanian and Q. Ma, Review on the strategies to improve the mechanical strength of highly porous bone bioceramic scaffolds, *J. Eur. Ceram. Soc.*, 2024, **44**, 23–42.

39 F. Lu, R. Wu, M. Shen, L. Xie, M. Liu, Y. Li, S. Xu, L. Wan, X. Yang, C. Gao and Z. Gou, Rational design of bioceramic scaffolds with tuning pore geometry by stereolithography: microstructure evaluation and mechanical evolution, *J. Eur. Ceram. Soc.*, 2021, **41**, 1672–1682.

40 H. Zhao, L. Li, S. Ding, C. Liu and J. Ai, Effect of porous structure and pore size on mechanical strength of 3D-printed comby scaffolds, *Mater. Lett.*, 2018, **223**, 21–24.

41 M. Zhang, X. Li, M. Zhang, Z. Xiu, J. G. Li, J. Li, M. Xie, J. Chen and X. Sun, High-strength macro-porous alumina ceramics with regularly arranged pores produced by gelcasting and sacrificial template methods, *J. Mater. Sci.*, 2019, **54**, 10119–10129.

42 H. J. Kang, P. Makkar, A. R. Padalhin, G. H. Lee, S. B. Im and B. T. Lee, Comparative study on biodegradation and biocompatibility of multichannel calcium phosphate based bone substitutes, *Mater. Sci. Eng., C*, 2020, **110**, 110694.

43 H. Shao, Y. He, J. Fu, D. He, X. Yang, J. Xie, C. Yao, J. Ye, S. Xu and Z. Gou, 3D printing magnesium-doped wollastonite/β-TCP bioceramics scaffolds with high strength and adjustable degradation, *J. Eur. Ceram. Soc.*, 2016, **36**, 1495–1503.

44 X. Sun, X. Jiao, X. Yang, J. Ma, T. Wang, W. Jin, W. Li, H. Yang, Y. Mao, Y. Gan, X. Zhou, T. Li, S. Li, X. Chen and

J. Wang, 3D bioprinting of osteon-mimetic scaffolds with hierarchical microchannels for vascularized bone tissue regeneration, *Biofabrication*, 2022, **14**, 035008.

45 P. S. Lienemann, Q. Vallmajo-Martin, P. Papageorgiou, U. Blache, S. Metzger, A. S. Kiveliö, V. Milleret, A. Sala, S. Hoehnel, A. Roch, R. Reuten, M. Koch, O. Naveiras, F. E. Weber, W. Weber, M. P. Lutolf and M. Ehrbar, Smart hydrogels for the augmentation of bone regeneration by endogenous mesenchymal progenitor cell recruitment, *Adv. Sci.*, 2020, **7**, 1903395.

46 G. Lu, Y. Xu, Q. Liu, M. Chen, H. Sun, P. Wang, X. Li, Y. Wang, X. Li, X. Hui, E. Luo, J. Liu, Q. Jiang, J. Liang, Y. Fan, Y. Sun and X. Zhang, An instantly fixable and self-adaptive scaffold for skull regeneration by autologous stem cell recruitment and angiogenesis, *Nat. Commun.*, 2022, **13**, 2499.

47 Y. Chen, Y. Li, F. Lu and Z. Dong, Endogenous bone marrow-derived stem cell mobilization and homing for in situ tissue regeneration, *Stem Cells*, 2023, **41**, 541–551.

48 S. J. Wang, D. Jiang, Z. Z. Zhang, Y. R. Chen, Z. D. Yang, J. Y. Zhang, J. Shi, X. Wang and J. K. Yu, Biomimetic nano-silica–collagen scaffolds for in situ bone regeneration: Toward a cell-free, one-step surgery, *Adv. Mater.*, 2019, **31**, 1904341.

49 G. P. Rajalekshmy and M. R. Rekha, Strontium ion cross-linked alginate-g-poly (PEGMA) xerogels for wound healing applications: *in vitro* studies, *Carbohydr. Polym.*, 2021, **251**, 117119.

50 S. Chen, H. Wang, V. L. Mainardi, G. Talò, A. McCarthy, J. V. John, M. J. Teusink, L. Hong and J. Xie, Biomaterials with structural hierarchy and controlled 3D nanotopography guide endogenous bone regeneration, *Sci. Adv.*, 2021, **7**, eabg3089.

51 C. Yang, H. Ma, Z. Wang, M. R. Younis, C. Liu, C. Wu, Y. Luo and P. Huang, 3D printed wesselsite nanosheets functionalized scaffold facilitates NIR–II photothermal therapy and vascularized bone regeneration, *Adv. Sci.*, 2021, **8**, 2100894.

52 A. Marrella, T. Y. Lee, D. H. Lee, S. Karuthedom, D. Syla, A. Chawla, A. Khademhosseini and H. L. Jang, Engineering vascularized and innervated bone biomaterials for improved skeletal tissue regeneration, *Mater. Today*, 2018, **21**, 362–376.

53 Z. Wang, Q. Dai, H. Luo, X. Han, Q. Feng and X. Cao, Nano-vibration exciter: Hypoxia-inducible factor 1 signaling pathway-mediated extracellular vesicles as bioactive glass substitutes for bone regeneration, *Bioact. Mater.*, 2024, **40**, 460–473.

54 J. Li, D. Zhai, F. Lv, Q. Yu, H. Ma, J. Yin, Z. Yi, M. Liu, J. Chang and C. Wu, Preparation of copper-containing bioactive glass/eggshell membrane nanocomposites for improving angiogenesis, antibacterial activity and wound healing, *Acta Biomater.*, 2016, **36**, 254–266.

55 P. Wang, Y. Yuan, K. Xu, H. Zhong, Y. Yang, S. Jin, K. Yang and X. Qi, Biological applications of copper-containing materials, *Bioact. Mater.*, 2021, **6**, 916–927.

56 J. Zhang, J. Pan and W. Jing, Motivating role of type H vessels in bone regeneration, *Cell Proliferation*, 2020, **53**, e12874.

57 M. Chen, M. Li, X. Ren, F. Zhou, Y. Li, L. Tan, Z. Luo, K. Cai and Y. Hu, DNAzyme nanoconstruct-integrated autonomously-adaptive coatings enhance titanium-implant osteointegration by cooperative angiogenesis and vessel remodeling, *ACS Nano*, 2023, **17**, 15942–15961.

58 X. Yu, X. Wang, D. Li, R. Sheng, Y. Qian, R. Zhu, X. Wang and K. Lin, Mechanically reinforced injectable bioactive nanocomposite hydrogels for *in situ* bone regeneration, *Chem. Eng. J.*, 2022, **433**, 132799.

59 Y. Zhu, H. Liu, P. Wu, Y. Chen, Z. Deng, L. Cai and M. Wu, Multifunctional injectable hydrogel system as a mild photothermal-assisted therapeutic platform for programmed regulation of inflammation and osteo-microenvironment for enhanced healing of diabetic bone defects in situ, *Theranostics*, 2024, **14**, 7140.

60 M. Wu, H. Liu, Y. Zhu, P. Wu, Y. Chen, Z. Deng, X. Zhu and L. Cai, Bioinspired soft-hard combined system with mild photothermal therapeutic activity promotes diabetic bone defect healing *via* synergetic effects of immune activation and angiogenesis, *Theranostics*, 2024, **14**, 4014.

61 M. Wu, H. Liu, Y. Zhu, F. Chen, Z. Chen, L. Guo, P. Wu, G. Li, C. Zhang, R. Wei and L. Cai, Mild photothermal-stimulation based on injectable and photocurable hydrogels orchestrates immunomodulation and osteogenesis for high-performance bone regeneration, *Small*, 2023, **19**, 2300111.

62 M. Wu, H. Liu, D. Li, Y. Zhu, P. Wu, Z. Chen, F. Chen, Y. Chen, Z. Deng and L. Cai, Smart-responsive multifunctional therapeutic system for improved regenerative microenvironment and accelerated bone regeneration *via* mild photothermal therapy, *Adv. Sci.*, 2024, **11**, 2304641.

63 W. Dang, K. Yi, E. Ju, Y. Jin, Y. Xu, H. Wang, W. C. Chen, K. Wang, Y. Wang, Y. Tao and M. Li, 3D printed bioceramic scaffolds as a universal therapeutic platform for synergistic therapy of osteosarcoma, *ACS Appl. Mater. Interfaces*, 2021, **13**, 18488–18499.

64 Y. Fang, X. Luo, Y. Xu, Z. Liu, R. L. Mintz, H. Yu, X. Yu, K. Li, E. Ju, H. Wang, Z. Tang, Y. Tao and M. Li, Sandwich-structured implants to obstruct multipath energy supply and trigger self-enhanced hypoxia-initiated chemotherapy against postsurgical tumor recurrence and metastasis, *Adv. Sci.*, 2023, **10**, 2300899.